Energies **2015**, *8*, 6427-6450; doi:10.3390/en8076427

OPEN ACCESS

energies

ISSN 1996-1073

www.mdpi.com/journal/energies

Article

Single-Source Multi-Battery Solar Charger: Analysis and Stability Issues

Alon Kuperman [1,*], Moshe Sitbon [1], Shlomo Gadelovits [1], Moshe Averbukh [1] and Teuvo Suntio [2]

[1] Department of Electrical Engineering and Electronics, Ariel University, Ariel 40700, Israel; E-Mails: sitbon222@gmail.com (M.S.); shlomoga@ariel.ac.il (S.G.); mosheav@ariel.ac.il (M.A.)

[2] Department of Electrical Engineering, Tampere University of Technology, Tampere FI-33101, Finland; E-Mail: teuvo.suntio@tut.fi

* Author to whom correspondence should be addressed; E-Mail: alonku@ariel.ac.il; Tel.: +972-526-943-234; Fax: +972-390-662-38.

Academic Editor: Andrés Muñoz

Received: 8 May 2015 / Accepted: 17 June 2015/ Published: 25 June 2015

Abstract: In this paper, dynamic analysis of a multi-battery dual mode charger, powered by a single solar array and suitable for lead-acid and lithium-ion cell-based batteries is presented. Each battery is interfaced to the solar array by means of a current-controlled buck power stage, operating either in constant power or constant voltage mode. Operation in former/latter charging mode implies regulating input/output voltage of the converter, which is a non-trivial situation since while feeding different batteries, all the converters share the same input terminals, connected to the solar array. It is revealed that when at least one of the batteries operates in constant power charging mode, open-loop instability occurs whenever converter input voltage is lower than maximum power point voltage of the solar array. Consequently, input voltage regulating controller must be designed to stabilize closed-loop dynamics for the worst case of instability, which is also derived. Moreover, it is shown that the dynamics of the converters operating under output voltage control are perceived as disturbances by input voltage control loop and must be properly rejected. Simple loop shaping design is proposed based on a PI controller, allowing stabilizing the system in case of worst case instability and rejecting output voltage control induced disturbances at the expense of non-constant, operating-point dependent closed-loop damping.

Keywords: battery charging; photovoltaic converters; small-signal modeling; input voltage control; stability assessment

1. Introduction

The intermittent nature of photovoltaic sources limits their operation to systems with sufficient storage capacity. In grid-connected photovoltaic installations, the electrical network is perceived as a nearly-infinite storage capacity device, capable of absorbing all the energy generated by a solar array (SA). On the contrary, off-grid systems (often referred to as microgrids) fed by photovoltaic sources require careful sizing and energy management aimed to instantaneously match generation, storage and consumption [1–8].

In both the abovementioned cases, the photovoltaic source is usually connected to a voltage-source type storage (battery or voltage-regulated capacitor) via a power processing interface (DC-DC converter). In grid-connected installation, the system operates solely in maximum power point tracking mode to harvest as much photovoltaic energy as possible [9], while in off-grid case power limiting operation (in which the amount of harvested photo-energy is lower than that available) may occur in the case that the microgrid's power consuming abilities are limited [10]. The mentioned DC-DC converter is often referred to as "charger" since its operation is usually independent on whether the storage element is connected to other devices or not.

Photovoltaic chargers should be implemented using single-conversion-stage topology to increase efficiency [11–14], capable of performing two following main tasks: managing the SA-generated power, while complying with the charging requirements of the voltage-source-type load [15,16]. The main charging requirements are overcurrent and overvoltage protection in order to avoid thermal runaways, accelerated ageing and other malfunctions of batteries and capacitors. As a result, photovoltaic chargers should attempt to maximize harvested photovoltaic energy yet keeping the absorbing device operation within allowed limits. Consequently, modern battery/capacitor chargers must be capable of dual mode operation: maximum power tracking (as long as the storage device is capable of absorbing the whole generated power) and power limiting (once the absorbing capabilities of storage device are lower than generated power).

A common off-grid solar charger application is powering portable electronics batteries (laptops, cell-phones, *etc*.), operating at relatively low voltages (the only exception is perhaps electric vehicle batteries, operating at several hundred volts [17]). In order to form a SA with sufficient rated power, multiple cells are connected (usually in series). As a result, the nominal operating array voltage is usually higher than the portable electronics' equipment battery voltage, necessitating the use of buck converters as power electronics interfaces. In addition, since current control (either peak or average) has become a very popular method due to the desirable features it provides, such as nearly first-order control dynamics of the voltage loop, high attenuation of input voltage disturbances and inherent current limiting, most of the modern PWM control IC's include current-mode-controller circuitry. Consequently, current-controlled buck power stages are considered in this paper as power processing interfaces, opposed to the conventional boost power stages typically used in grid-connected photovoltaic

systems. Nevertheless, unlike in boost converter based power stages, stability issues were shown to arise when utilizing current-controlled buck converters as power electronic interfaces in photovoltaic applications [18,19] because of interactions between converter dynamics and solar array impedance [20], leading to open-loop instability.

When multiple batteries are fed by a single panel, typical photovoltaic charging arrangement include a single power processing interface feeding a common DC bus, supplying the rest of the consumers via their own power converters [11] as demonstrated in Figure 1a. The SA-interfacing converter is in charge for harvesting the maximum available SA power (via v_I regulation) while battery converters' task is transferring this power into the batteries by regulating the voltage v_B. Consequently, SA and batteries dynamics is decoupled. In this paper, a different approach is discussed. Here, all the consumers are connected directly to the SA via their power processing interfaces. The system under consideration in this paper is shown in Figure 1b, presenting N batteries, requiring dual-stage charging, powered from a single SA via N DC-DC power converters. Converter input currents, output currents and output (*i.e.*, battery terminal) voltages are denoted by i_{I1}, … , i_{IN}, i_{O1}, … , i_{ON} and v_{O1}, … , v_{ON}, respectively. All the converters share input terminals with SA output terminals, whose voltage is symbolized by v_I.

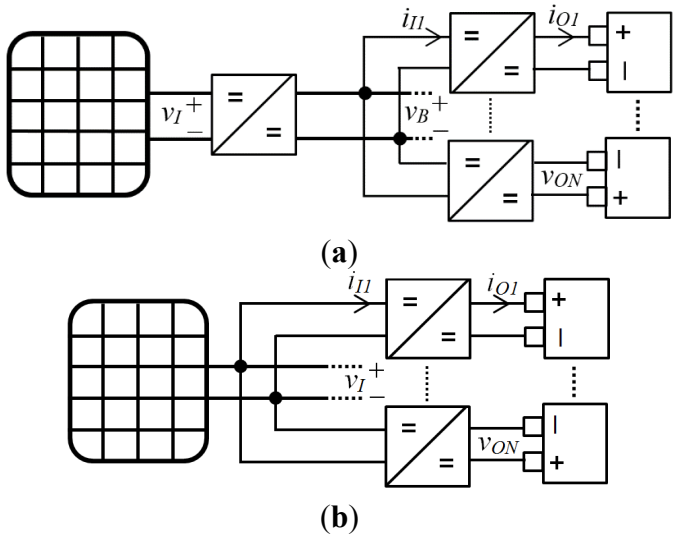

Figure 1. Single source multi battery solar charger topologies: (**a**) typical; (**b**) proposed.

Reducing the number of conversion stages decreases the system cost and physical size while increasing efficiency. On the other hand, coupling SA and batteries dynamics introduces additional control issues.

In this paper, dynamic analysis of a multi-battery dual mode charger, powered by a single SA is presented; both single and multi-battery cases are investigated. The single-battery case extends the work described in [19] by deriving worst-case instability condition in terms of transfer function, explicitly quantifying the unstable pole frequency and thus defining the set point for stabilizing controller design. Then, the proposed method is extended to a general multi-battery case, revealing that while the factor leading to instability remains the same, cross-couplings between the converters occur, introducing both additional disturbances and altering the instability characteristics. Simple controller design is proposed, allowing stabilizing the loop for the worst-case instability while rejecting the disturbances caused by the control loops cross-coupling.

The topic under consideration may be referred to as a problem contrary to load sharing [21,22], where a single load is to be allocated among several sources. Here, a single source is shared by several loads. It is important to emphasize that to the best of authors' knowledge, source sharing in general and single-SA multi-battery charger in particular were not treated in the literature by far, hence this may be considered a relatively novel contribution.

The rest of the manuscript is arranged as follows: Section 2 presents a single-array single battery case analysis, aimed to reveal mechanisms of dual-stage battery charging. Extension to multi-battery case is carried out in Section 3, followed by controller design, discussed in Section 4. Sample results are shown in Section 5. The manuscript is concluded in Section 6.

2. Single Battery Case

In order to clarify the underlying mechanisms of dual-stage battery charging from a photovoltaic generator, the single-SA single-battery arrangement shown in Figure 2 is analyzed first.

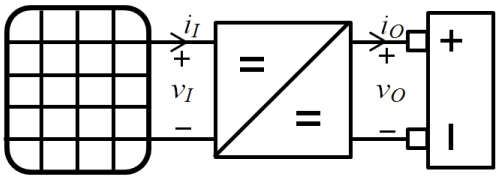

Figure 2. Single solar array single battery arrangement.

2.1. Operating Modes

The system may operate in one of the two modes as follows: as long as the battery terminal voltage is below its rated value (*e.g.*, 4.2 V per cell in case of a typical Li-Ion battery), the SA should be operating at maximum power point (MPP), transferring as much energy as possible to the battery. This operation mode is usually referred to as "constant power" (CP) charging mode and converter input voltage v_I is typically regulated, as shown in Figure 3a. The reference value of input voltage is created by an MPP tracker (MPPT); moreover, since battery terminal voltage may be considered constant during the MPPT algorithm convergence period, MPP tracking implies maximizing the current injected into the battery, *i.e.*, a single-sensor MPPT [23] algorithm should be utilized. In addition, when output rather than input converter variables are used to implement MPPT, converter efficiency is automatically taken into account [24]. Since current mode controlled converters are considered in the paper, the voltage controller output is actually the reference command to the current controller, which in turn creates converter switches operating duty cycles. The power flow diagram of the system, operating in CP mode is shown in Figure 4a. The power, generated by SA is transferred to the battery side (taking into account converter efficiency η) as $P_B = \eta \cdot P_{PV}$. Consequently, battery charging current is given by the solution of the following quadratic equation:

$$P_B = R_{BAT} i_O^2 + V_{BAT} i_O \tag{1}$$

where R_{BAT} and V_{BAT} are battery equivalent series resistance and internal voltage, respectively, depending on battery temperature, age and state of charge.

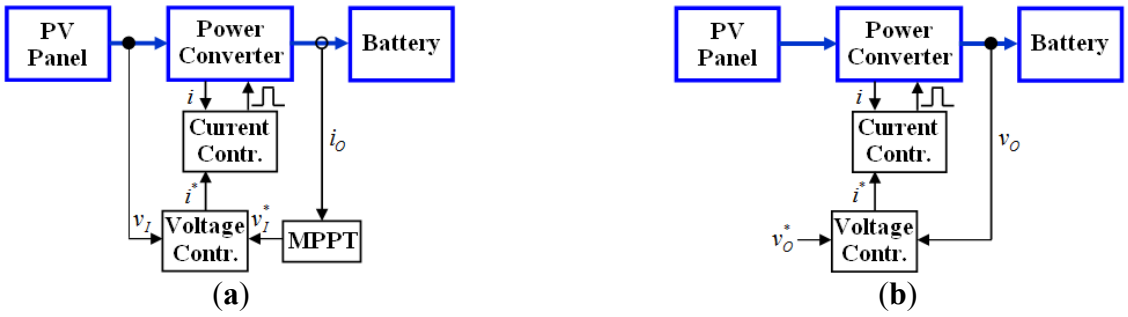

Figure 3. Control structure of (**a**) constant power (CP) mode; (**b**) constant voltage (CV) mode.

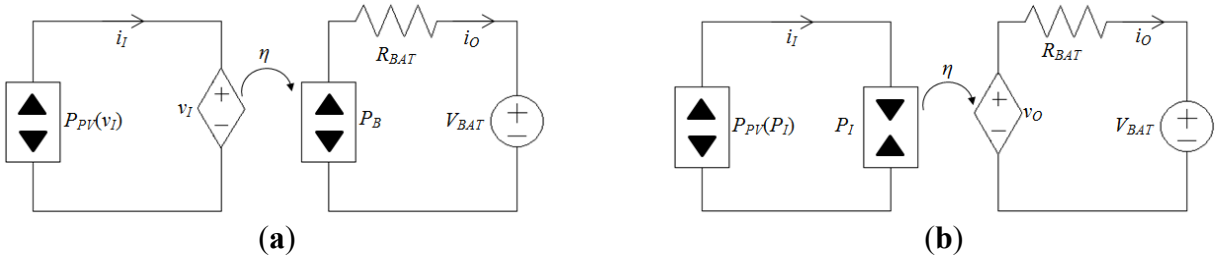

Figure 4. Power flow diagrams of (**a**) CP mode; (**b**) CV mode.

When the battery terminal voltage reaches its rated value, the system switches to the second operating mode, usually referred to as "constant voltage" (CV) charging mode. In this mode, the converter output voltage v_O is regulated to the rated voltage of the employed battery, as shown in Figure 3b. Consequently, charging current (and hence charging power) is determined by the battery as:

$$i_O = \frac{v_O - V_{BAT}}{R_{BAT}}. \tag{2}$$

Charging power is reflected from the SA side (taking into account converter efficiency η) as (cf. Figure 4b):

$$P_I = \frac{v_O i_O}{\eta} = \frac{v_O \left(v_O - V_{BAT}\right)}{\eta R_{BAT}}. \tag{3}$$

Consequently, the SA array operating point is determined by intersection of its P-V curve with constant power P_I. Moreover, output voltage controller again creates reference command to the current controller. Therefore, the same current controller may be utilized for both operating modes, as shown in Figure 5, where the reference current fed to the current controller is determined by operation mode selector.

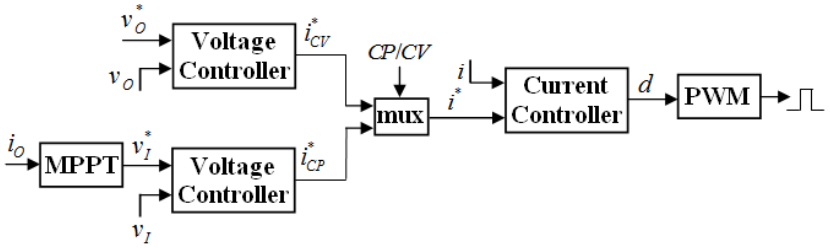

Figure 5. Single battery dual-mode control structure.

In the CP mode the SA is MPP-operated, extracting maximum available power $P_{PV,MAX}$ which is delivered to the batteries (scaled by converter efficiency), as shown in Figure 6. On the other hand, the SA is limited power point (LPP)—operated in the CV mode, since battery power absorbing capabilities are bounded there to prevent overvoltage (leading to accelerated ageing, thermal runaway, *etc.*). Consequently, less than maximum available power $P_{PV,MAX}$ is extracted from the SA in CV mode. Two following issues, related to non-MPP operation, must be highlighted.

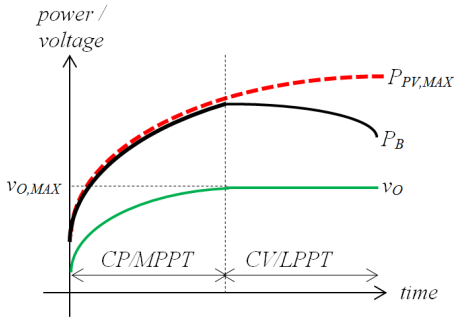

Figure 6. Operating modes.

2.1.1. Static Instability

At the instant of CP-to-CV mode transition, SA is MPPT-operated, *i.e.*, charging power PB equals maximum available power $P_{PV,MAX}$ (assuming lossless conversion), corresponding to (v_{MAX}, i_{MAX}) and (v_{MAX}, $P_{PV,MAX}$) operating points in I-V and P-V planes, respectively (cf. Figure 7). As the battery replenishes, charging power reduces since V_{BAT} rises while v_O remains constant. Consequently, when charging power becomes lower than maximum available power, two static operating points exist, possessing similar power $P_{B,CV}$ at two different voltages v_1 and v_2. Assuming that SA is terminated by a capacitor C_I and referring to Figure 4b, input power flow dynamics is governed by the following relation:

$$P_{PV} - P_I = C_I \frac{dv_I}{dt} v_I. \quad (4)$$

Note that v_I is a positive variable, hence the polarity of Equation (4) dictates the sign of input voltage time-derivative. Consider the case where instantaneous operating point is $v_I = v_1$ and a small positive (negative) perturbation Δv is added to v_I. As a result, P_{PV} rises (decreases) while P_I remains unchanged, leading to positive (negative) $\frac{dv_I}{dt}$, forcing v_I to recede from v_1. Consequently, the operating point residing to the left of MPP (corresponding to v_1) is unstable. It is important to emphasize that non-MPP operation may occur not only during CV mode but also during CP mode upon rapid solar irradiation change, therefore under proper control, the system in steady state should settle to the right of MPP (corresponding to v_2, which can be proven to be stable using similar analysis).

2.1.2. Operation Point Loss

If during CV mode irradiation reduces such that maximum available power $P_{PV,MAX}$ is lower than charging power P_B, no operation point would exist (see Figure 7) and SA voltage collapse to zero according to Equation (4). Therefore, such situation must be properly detected and the system should

immediately switch back to CP mode to preserve operating point (note that such phenomenon does not take place in conventional, off-grid battery chargers [25]).

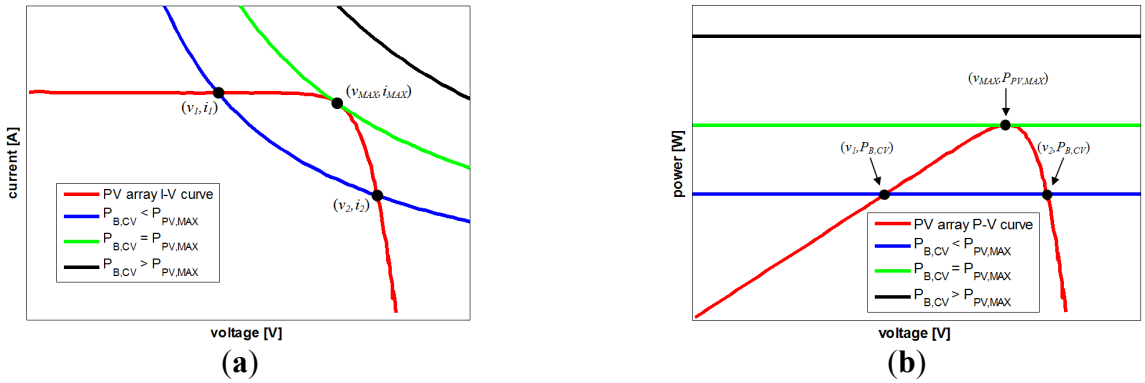

(a) **(b)**

Figure 7. Solar Array (SA) operating points: (**a**) I-V plane; (**b**) P-V plane.

2.2. Solar Array (SA) Modeling for Large and Small Signal Analysis

Referring to the single-diode equivalent circuit of a SA shown in Figure 8, the model contains irradiation and temperature dependent photocurrent source I_{PH}, semiconductor diode D (symbolizing recombination losses) and equivalent shunt and series resistances R_{SH} and R_S, respectively [26]. Consequently, SA current is given by:

$$I = I_{PH} - I_D - \frac{V + IR_S}{R_{SH}} \tag{5}$$

Diode behavior is governed by Shockley Equation:

$$I_D = I_0 (e^{\frac{V+IR_S}{aV_T}} - 1) \tag{6}$$

where I_0 and a are temperature dependent reverse saturation current and diode ideality factor, respectively and V_T is thermal voltage.

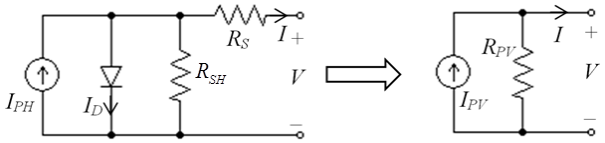

Figure 8. SA equivalent circuit and its Norton equivalent.

In order to be suitable for small-signal analysis, the SA equivalent circuit should be linearized and consequently represented by Norton equivalent. Norton resistance (which is actually SA dynamic resistance) and current are then given by:

$$R_{PV} = R_S + R_{SH} \parallel R_D = R_S + \left(R_{SH}^{-1} + \frac{I_0}{N_S V_T \eta} e^{\frac{V+IR_S}{aV_T N_S}} \right)^{-1} \tag{7}$$

and

$$I_{PV} = I_{PH} \frac{R_{SH} \parallel R_D}{R_S + R_{SH} \parallel R_D} \tag{8}$$

respectively, where R_D denotes semiconductor diode dynamic resistance [27,28] and N_S symbolizes the number of series-connected cells, forming the SA. Therefore, the linearized version of Equation (5) is given by:

$$I = I_{PV} - R_{PV}^{-1} V \tag{9}$$

Note that both R_{PV} and I_{PV} are operating point as well as environmental variables dependent, *i.e.*, Equation (9) varies with operating point, temperature and irradiation.

2.3. System Analysis

Switching cycle averaged model of the system is shown in Figure 9, governed by the following set of equations (continuous conduction mode is assumed):

$$\begin{aligned} C_I \frac{dv_I}{dt} &= I_{PV} - \frac{v_I}{R_{PV}} - di_L \\ L \frac{di_L}{dt} &= dv_I - v_O \\ C_O \frac{dv_O}{dt} &= i_L - \frac{v_O - V_{BAT}}{R_{BAT}} \end{aligned} \tag{10}$$

Perturbing the time-based variables as $v_I = V_I + \tilde{v}_I$, $d = D + \tilde{d}$, $i_L = I_L + \tilde{i}_L$, $v_O = V_O + \tilde{v}_O$, small-signal representation of the system is obtained as:

$$\begin{aligned} C_I \dot{\tilde{v}}_I &= -R_{PV}^{-1} \tilde{v}_I - I_L \tilde{d} - D\tilde{i}_L \\ L \dot{\tilde{i}}_L &= D\tilde{v}_I + V_I \tilde{d} - \tilde{v}_O \\ C_O \dot{\tilde{v}}_O &= \tilde{i}_L - R_{BAT}^{-1} \tilde{v}_O \end{aligned} \tag{11}$$

linearized around an operating point given by (assuming lossless conversion):

$$\begin{aligned} \frac{P_{PV}}{V_I} &= I_{PV} - V_I R_{PV}^{-1} = DI_L \\ DV_I &= V_O \\ \frac{P_{PV}}{V_O} &= I_L = \left(V_O - V_{BAT}\right) R_{BAT}^{-1} \end{aligned} \tag{12}$$

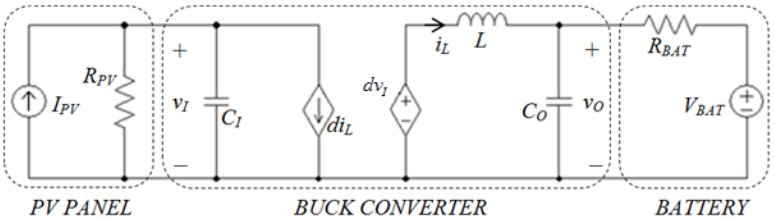

Figure 9. Averaged system model.

In the case of a current-controlled buck converter, current loop bandwidth is usually much higher than voltage loop bandwidth; therefore when shaping the voltage loop, equality of commanded and actual current may be assumed. In case of average current control, this implies that inductor average current perfectly follows current reference, created by the voltage controller. On the other hand, in case of peak current mode control (CMC), average inductor current differs from the current reference (denoting peak rather than average inductor current value) and is given by [29]:

$$i_L = i^* - \frac{1}{2LF_s}\frac{v_O}{v_I}\left(2mL + v_I - v_O\right) = i^* - \Delta i, \tag{13}$$

where F_s and m are switching frequency and compensation ramp slope, respectively.

Nevertheless, as shown in Figure 10, Δi may be treated as slow-varying disturbance, which will be rejected in steady state by voltage controller, and hence inductor average current may be assumed to follow current reference precisely. Subsequently, substituting $\tilde{\imath}_L \cong \tilde{\imath}_L^*$ and $I_L \cong I_L^*$ into Equations (11) and (12), respectively, the averaged large-signal system model may be re-drawn as shown in Figure 11.

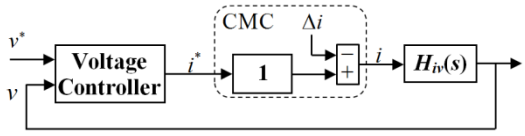

Figure 10. Current tracking in case of current mode control (CMC).

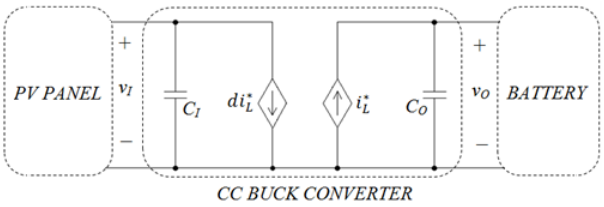

Figure 11. Averaged current-controlled system model.

Further manipulating and applying Laplace transform, inductor current reference-to-input and output voltages transfer functions are obtained as:

$$\frac{\tilde{v}_I}{\tilde{i}_L^*}(s) = -\frac{LC_O s^2 + \left(LR_{BAT}^{-1} + C_O D\right)s + \left(1 + R_{BAT}^{-1} D\left(I_L^*\right)^{-1} V_I\right)}{\left(I_L^*\right)^{-1} V_I \left(C_I s + R_{PV}^{-1} - I_L^* V_I^{-1} D\right)\left(C_O s + R_{BAT}^{-1}\right)} \tag{14}$$

and:

$$\frac{\tilde{v}_O}{\tilde{i}_L^*}(s) = \frac{1}{C_O s + R_{BAT}^{-1}}, \tag{15}$$

respectively. Furthermore, defining SA static resistance as:

$$R_I \overset{\Delta}{=} \frac{V_I}{I_I} = V_I\left(DI_L^*\right)^{-1}, \tag{16}$$

Equation (14) may be rearranged as:

$$\frac{\tilde{v}_I}{\tilde{i}_L^*}(s) = -G\frac{\left(\omega_{Z1}^{-1}s+1\right)\left(\omega_{Z2}^{-1}s+1\right)}{\left(\omega_{PV}^{-1}s+1\right)\left(\omega_{BAT}^{-1}s+1\right)} \tag{17}$$

with

$$\begin{gathered} G = \frac{R_{BAT}+D^2R_I}{D\left(R_IR_{PV}^{-1}-1\right)} \\ \omega_{PV}^{-1} = C_I\left(R_{PV}^{-1}-R_I^{-1}\right)^{-1}, \quad \omega_{Z1}^{-1}\omega_{Z2}^{-1} = LC_O\left(1+D^2R_IR_{BAT}^{-1}\right)^{-1} \\ \omega_{BAT}^{-1} = C_OR_{BAT}, \quad \omega_{Z1}^{-1}+\omega_{Z2}^{-1} = \left(LR_{BAT}^{-1}+C_OD^2R_I\right)\left(1+D^2R_IR_{BAT}^{-1}\right)^{-1} \end{gathered} \tag{18}$$

The inductor current reference-to-output voltage transfer function given by Equation (15) implies that the plant in CV mode behaves as a first order system with relatively constant parameters (battery resistance may vary slowly during charging). Moreover, while static operation point exists, *i.e.*, CV-operated battery charging power is lower than maximum available photovoltaic power, Equation (15) is operating point and environmental conditions independent. On the other hand, inductor current reference–to-input voltage transfer function defined by Equation (17) is non-trivial. First, note the negative gain, requiring negative controller gain to ensure closed-loop stability. Second, while both zeros and battery induced pole reside in the left-hand plane (LHP), the pole ω_{PV} moves to the right-hand plane (RHP) when SA dynamic resistance R_{PV} is higher than SA static resistance R_I. Note that the following holds at MPP:

$$\left.\frac{dP_{PV}}{dv_I}\right|_{MPP} = 0 = \left.\frac{d(v_Ii_I)}{dv_I}\right|_{MPP} = V_M\left.\frac{di_I}{dv_I}\right|_{MPP} + I_M \tag{19}$$

with (V_M, I_M) denoting MPP coordinates, leading to:

$$R_{PV}\big|_{MPP} \overset{\Delta}{=} -\left.\frac{dv_I}{di_I}\right|_{MPP} = \frac{V_M}{I_M} \overset{\Delta}{=} R_I\big|_{MPP}, \tag{20}$$

i.e., static and dynamic resistances coincide at MPP [30]. Consequently, for voltages below v_M dynamic resistance increases while static resistance decreases and the plant becomes open-loop unstable. On the other hand, for voltages above v_M dynamic resistance decreases while static resistance rises and the plant turns out to be open-loop stable.

Consider a SA I-V curve shown in Figure 12, with I_{SC} and V_{OC} denoting SA short-circuit current and open-circuit voltage, respectively. Since for proper operation of buck converter, input voltage must remain above output voltage, a minimum input voltage $V_{min} > 0$ would always exist. Consequently, converter input voltage is bounded by $V_{min} \le v_I \le V_{OC}$ and corresponding static and dynamic (cf. Equation (7)) resistances are given by:

$$R_I \cong \begin{cases} \infty, & v_I = V_{OC} \\ V_MI_M^{-1}, & v_I = V_M \\ V_{min}I_{SC}^{-1}, & v_I = V_{min} \end{cases} \tag{21}$$

and:

$$R_{PV} \cong \begin{cases} R_S, & v_I = V_{OC} \\ V_M I_M^{-1}, v_I = V_M \\ R_S + R_{SH}, v_I = V_{min} \end{cases} \tag{23}$$

leading to the following SA induced pole:

$$\omega_{PV} \approx C_I^{-1} \begin{cases} R_{PV}^{-1}, & v_I = V_{OC} \\ 0, & v_I = V_M \\ -R_I^{-1}, v_I = V_{\min} \end{cases} = \begin{cases} \left(C_I R_S\right)^{-1}, & v_I = V_{OC} \\ 0, & v_I = V_M \\ -I_{SC}\left(C_I V_{min}\right)^{-1}, v_I = V_{\min} \end{cases} \tag{24}$$

Subsequently, the worst case instability is characterized by:

$$\omega_{PV\min} = -\left(C_I R_{Imin}\right)^{-1} \approx -I_{SC}\left(C_I V_{min}\right)^{-1} \tag{25}$$

i.e., the input voltage controller should be designed to stabilize the closed-loop system for this value since closed loop stability in the worst-case implies stability in all operating region. It is important to emphasize though that open-loop instability can be avoided in case of current-mode-controlled converter by increasing compensating ramp slope m in Equation (13), as recently demonstrated in [19]. Nevertheless, if the compensating ramp slope is inaccessible or absent (as in case of average-mode controlled converter), the open-loop instability region is unavoidable and must appropriately treated by the feedback controller.

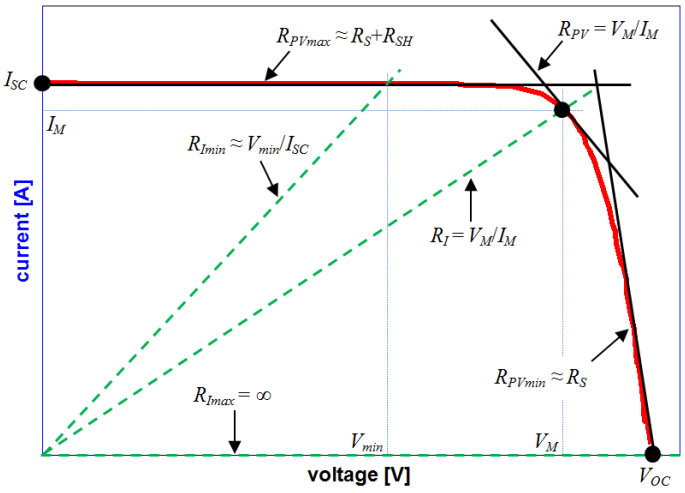

Figure 12. Determining open-loop instability region.

3. Extension to Multi-Battery Case

Now, consider the arrangement in Figure 1. Assume that the SA powers N batteries through N current-controlled buck converters, out of which batteries 1…M operate in CP mode, batteries K…N operate in CV mode and batteries $M+1$…$K-1$ are disconnected. The power flow diagram of the system is shown in Figure 13 (assuming lossless conversion).

The power drawn by each battery is:

$$P_{B,i} = \begin{cases} \alpha_i \left(P_{PV} - P_B \right), \; i = 1 \ldots M \\ V_{O,i} \left(V_{O,i} - V_{BAT,i} \right) R_{BAT,i}^{-1}, \; i = K \ldots N \end{cases} \tag{26}$$

where P_B is the total power of CV-operated batteries:

$$P_B = \sum_{i=K}^{N} P_{BAT,i}, \tag{27}$$

and α_i is scaling factor, determined by relative rating of i-th converter with:

$$\sum_{i=1}^{M} \alpha_i = 1. \tag{28}$$

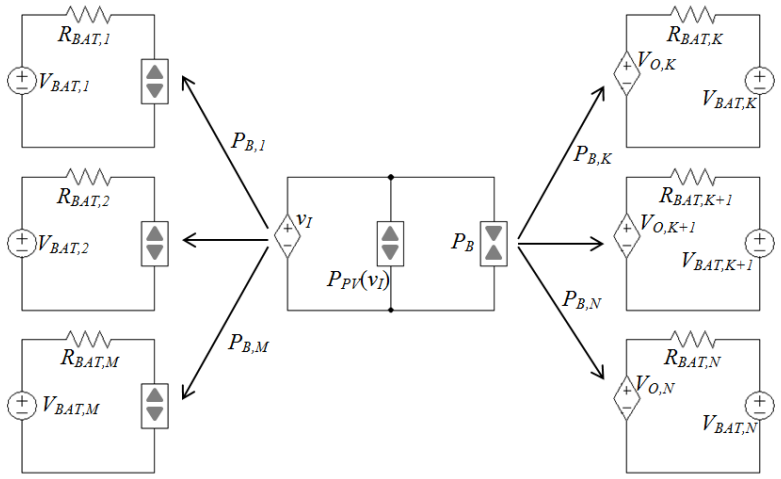

Figure 13. Power flow diagram of a multi-battery system.

Overall control structure is shown in Figure 14. Note that the reference current of each converter, feeding a CP-operated battery, is determined by appropriate scaling (according to Equations (26) and (28)) of total reference current i^*, created by the input voltage controller.

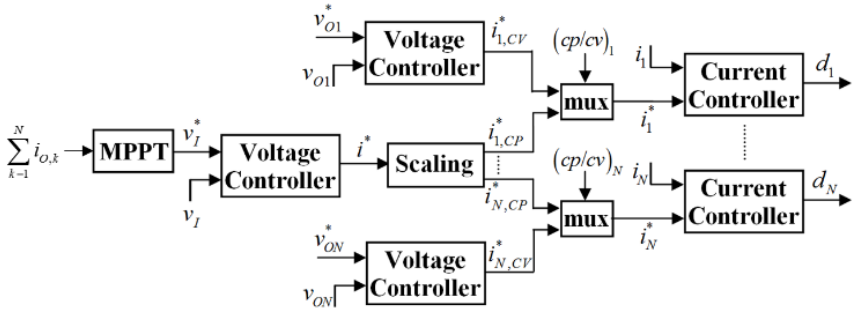

Figure 14. Multi-battery dual-mode control structure.

Switching cycle averaged model of the system is shown in Figure 15, governed by the following set of equations:

$$C_I \frac{dv_I}{dt} = I_{PV} - \frac{v_I}{R_{PV}} - \sum_{k=1}^{N} d_k i_{Lk}$$
$$L_k \frac{di_{Lk}}{dt} = d_k v_{PV} - v_{Ok} \quad (29)$$
$$C_{Ok} \frac{dv_{Ok}}{dt} = i_{Lk} - \frac{v_{Ok} - V_{BATk}}{R_{BATk}}$$

for $k = 1 \ldots N$. Perturbing the time-based variables as $v_I = V_I + \tilde{v}_I$, $d_k = D_k + \tilde{d}_k$, $i_{Lk} = I_{Lk} + \tilde{i}_{Lk}$, $v_{Ok} = V_{Ok} + \tilde{v}_{Ok}$, small-signal representation of the system is obtained as:

$$C_I \dot{\tilde{v}}_I = -R_{PV}^{-1} \tilde{v}_I - I_{L1} \tilde{d}_1 - D_1 \tilde{i}_{L1} - I_{L2} \tilde{d}_2 - D_2 \tilde{i}_{L2}$$
$$L_k \dot{\tilde{i}}_{Lk} = D_k \tilde{v}_I + V_I \tilde{d}_k - \tilde{v}_{Ok} \quad (30)$$
$$C_{Ok} \dot{\tilde{v}}_{Ok} = \tilde{i}_{Lk} - R_{BATk}^{-1} \tilde{v}_{Ok}$$

linearized around an operating point given by (assuming lossless conversion):

$$\frac{P_{PV}}{V_I} = I_{PV} - V_I R_{PV}^{-1} = \sum_{k=1}^{N} D_k I_{Lk}$$
$$D_k V_I = V_{Ok} \quad (31)$$
$$\frac{P_{Ok}}{V_{Ok}} = I_{Lk} = \left(V_{Ok} - V_{BATk}\right) R_{BATk}^{-1}$$

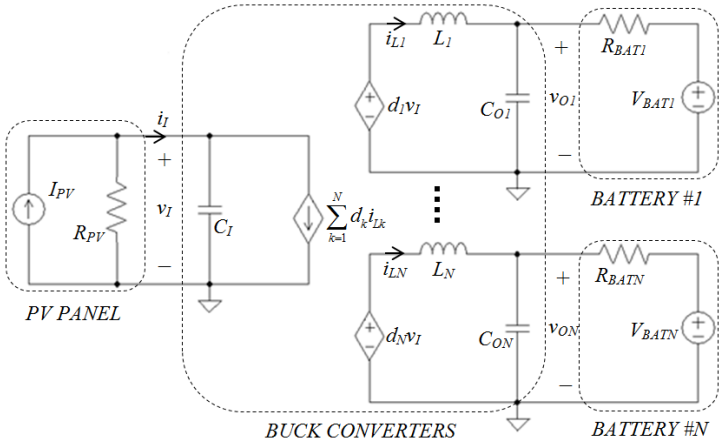

Figure 15. Large-signal system model.

Accounting for current-control by substituting $\tilde{\imath}_{Lk} \cong \tilde{\imath}_{Lk}^* = \alpha_k \tilde{\imath}_L^*$ and $I_{Lk} \cong I_{Lk}^* = \alpha_k I_L^*$ into Equations (30) and (31), respectively, the averaged large-signal system model may be re-drawn as shown in Figure 16. Applying Laplace transform to Equation (30), inductor current reference-to-output voltage transfer function of *k*-th converter, feeding a CV-operated battery is obtained as:

$$P_{Ok}(s) = \frac{\tilde{v}_{Ok}}{\tilde{i}_{Lk}^*}(s) = \frac{1}{C_{Ok} s + R_{BATk}^{-1}}. \quad (32)$$

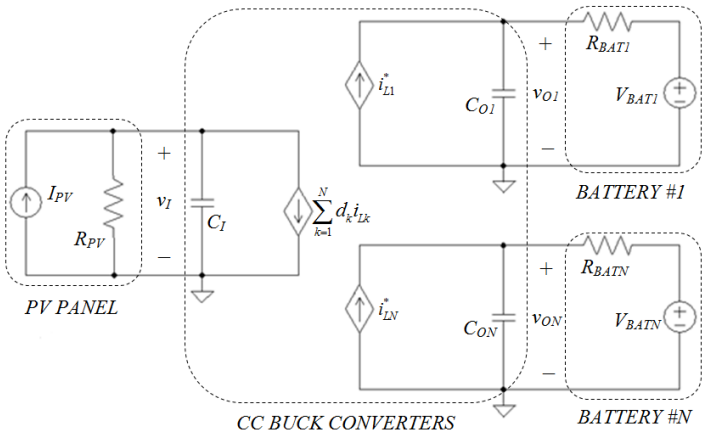

Figure 16. Large-signal current-controlled system model.

As in the single-battery case, if CV-operated battery charging power is lower than maximum available photovoltaic power, $P_{Ok}(s)$ is operating point and environmental conditions independent. As to input voltage small-signal dynamics, note that according to Figure 14, input-voltage side closed-loop system may be represented by Figure 17, *i.e.*, reference voltage commands of converters feeding CV-operated batteries (v_{Ok}^*, $k = K…N$), act as disturbances on the input voltage loop. Consequently, input-voltage dynamics is of the following form:

$$\tilde{v}_I(s) = H_{IV}(s)\tilde{i}_L^*(s) + \sum_{k=K}^{N} H_{VVk}(s)\tilde{v}_{Ok}^*(s). \tag{33}$$

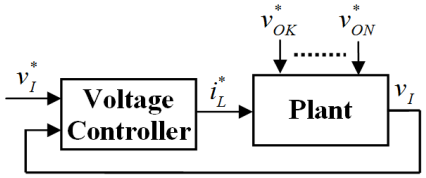

Figure 17. Input voltage side closed loop system.

Inductor current reference-to-input voltage transfer function is obtained by manipulating Equation (30) as:

$$H_{IV}(s) = \left.\frac{\tilde{v}_I}{\tilde{i}_L^*}(s)\right|_{\tilde{v}_{Ok}^*=0,k=K\ldots N} = -\sum_{k=1}^{M} G_k \frac{\left(\omega_{Z1k}^{-1}s+1\right)\left(\omega_{Z2k}^{-1}s+1\right)}{\left(\omega_{PV}^{-1}s+1\right)\left(\omega_{BATk}^{-1}s+1\right)} \tag{34}$$

with:

$$\begin{gathered} G_k = \frac{\alpha_k R_{BATk}\left(1+D_k^2 R_{BATk}^{-1} R_{Ik}\right)}{D_k R_{Ik}\left(R_{PV}^{-1}-R_I^{-1}\right)} \\ \omega_{PV}^{-1} = C_I\left(R_{PV}^{-1}-R_I^{-1}\right)^{-1}, \quad \omega_{Z1k}^{-1}\omega_{Z2k}^{-1} = L_k C_{Ok}\left(1+D_k^2 R_{BATk}^{-1} R_{Ik}\right)^{-1} \\ \omega_{BATk}^{-1} = C_{Ok} R_{BATk}, \quad \omega_{Z1k}^{-1}+\omega_{Z2k}^{-1} = \left(L_k R_{BATk}^{-1} + C_{Ok} D_k^2 R_{Ik}\right)\left(1+D_k^2 R_{BATk}^{-1} R_{Ik}\right)^{-1} \end{gathered} \tag{35}$$

where:

$$R_I \overset{\Delta}{=} \frac{V_I}{I_I} = \frac{V_I}{\sum_{k=1}^{N} D_k I_{Lk}^*} \tag{36}$$

and:

$$R_{Ik} \overset{\Delta}{=} \frac{V_I}{D_k I_{Lk}^*}. \tag{37}$$

Note that for $M = 1$, Equation (34) reduces to Equation (17). Output voltage reference of k-th CV operating converter-to-input voltage transfer function is obtained from Equation (30) as:

$$H_{VVk}(s) = \frac{\tilde{v}_I}{\tilde{v}_{Ok}^*}(s)\Big|_{\tilde{i}_L^*=0,\tilde{v}_{On}^*=0,n=K\ldots N,n\neq k} = F_k \frac{\left(\omega_{Z1k}^{-1}s+1\right)\left(\omega_{Z2k}^{-1}s+1\right)}{\omega_{PV}^{-1}s+1} T_{Ok}^{CL}(s) \tag{38}$$

with:

$$F_k = \frac{1+D_k^2 R_{BATk}^{-1} R_{Ik}}{D_k R_{Ik}\left(R_{PV}^{-1}-R_I^{-1}\right)} \tag{39}$$

and:

$$T_{Ok}^{CL}(s) \overset{\Delta}{=} \frac{\tilde{v}_{Ok}}{\tilde{v}_{Ok}^*}(s)\Big|_{\tilde{i}_L^*=0,\tilde{v}_{On}^*=0,n=K\ldots N,n\neq k} \tag{40}$$

denoting the closed-loop k-th output voltage tracking transfer function, *i.e.*, if a controller $W_{Ok}(s)$ is selected to compensate the plant given by Equation (32), the closed-loop k-th output voltage tracking transfer function is given by:

$$T_{Ok}^{CL}(s) = \frac{W_{Ok}(s)P_{Ok}(s)}{1+W_{Ok}(s)P_{Ok}(s)}. \tag{41}$$

Despite multi-battery arrangement induced complications, stability-related issues remain similar to single-battery case. The only difference is that here all the converters contribute to SA static resistance, according to Equation (36). Consequently, the worst case instability is still characterized by Equation (25), setting the operating point for input voltage controller design.

4. Control Design

According to Equation (35), if $R_{BATk} << D^2 R_{Ik}$ (rather practical assumption), then $\omega_{Z2k} \approx \omega_{BATk}$ and $\omega_{Z1k} \approx L_k(D_k^2 R_{Ik})^{-1}$. Consequently, Equation (34) may be simplified by performing zero-pole cancellation and keeping the crossover frequency of input voltage loop much lower than ω_{Z1k} (which is relatively high for a small inductor) into:

$$H_{IV}(s) \approx -\frac{\sum_{k=1}^{M} G_{Ik}}{\omega_{PV}^{-1}s+1} \tag{42}$$

with:

$$G_{Ik} = \frac{\alpha_k D_k}{R_{PV}^{-1} - R_I^{-1}}. \tag{43}$$

Similarly, taking Equation (41) into account, Equation (38) reduces to:

$$H_{VVk}(s) \approx F_{Ok} \frac{W_{Ok}(s)}{1 + W_{Ok}(s) P_{Ok}(s)} \frac{1}{\omega_{PV}^{-1} s + 1} \tag{44}$$

with:

$$F_{Ok} = \frac{D_k}{R_{PV}^{-1} - R_I^{-1}}. \tag{45}$$

As a result, Equation (33) can be rearranged as:

$$\tilde{v}_I(s) = \frac{1}{\omega_{PV}^{-1} s + 1} \left(Q \tilde{i}_L^*(s) + \tilde{f}(s) \right) \tag{46}$$

where:

$$Q = -\frac{\sum_{k=1}^{M} \alpha_k D_k}{R_{PV}^{-1} - R_I^{-1}} \tag{47}$$

and:

$$\tilde{f}(s) = \left(\sum_{k=K}^{N} D_k \frac{W_{Ok}(s)}{1 + W_{Ok}(s) P_{Ok}(s)} \right) \tilde{v}_{Ok}^*(s). \tag{48}$$

are equivalent gain and disturbance, respectively. Assuming that $W_{Ok}(s)$ contains an integrator (e.g., proportional-integrative (PI) controller), and noticing that $\tilde{v}_{Ok}^*(t)$ is constant, it may be concluded that $\tilde{f}(s)$ is a low-frequency disturbance; hence input voltage loop controller should contain an integrator to reject it. Furthermore, taking into account Equation (25) and Figure 12, the worst case plant is given by:

$$H_{IV}^{WC}(s) = \frac{R_{I\min}}{\omega_{PV\min}^{-1} s + 1} \tag{49}$$

Hence, selecting e.g., a PI controller of the form:

$$W_I(s) = -\frac{K_P s + K_I}{s}, \tag{50}$$

as input voltage loop controller would be sufficient to assure steady-state disturbance rejection and lead to the following closed-loop tracking response:

$$T_I^{CL}(s) \overset{\Delta}{=} \frac{\tilde{v}_I}{\tilde{v}_I^*}(s)\bigg|_{\tilde{f}(s)=0} = \frac{-\omega_{PV\min} R_{I\min} \left(K_P s + K_I \right)}{s^2 + \omega_{PV\min} \left(1 - R_{I\min} K_P \right) s - \omega_{PV\min} R_{I\min} K_I}. \tag{51}$$

In order to stabilize Equation (51), the following must hold according to Routh-Horowitz criterion:

$$\begin{aligned} -\omega_{PV\min} R_{I\min} K_I &> 0 \\ \omega_{PV\min}\left(1 - R_{I\min} K_P\right) &> 0. \end{aligned} \tag{52}$$

while the first condition is always satisfied since $\omega_{PV\min} < 0$, proportional gain must be selected such that $K_P > R_{Imin}^{-1}$ in order to satisfy the second, *i.e.*, to keep the closed-loop bandwidth higher than twice the unstable pole frequency [31]. On the other hand, we remember that the closed-loop bandwidth should remain much lower than ω_{ZIk} in order to preserve the validity of Equations (42) and (44). Note that since there is no restriction on K_I, it should be selected to shape the transient response, since the plant does not remain constant when the operating point changes. The denominator of Equation (51) may be rewritten as:

$$\Delta_{CL}^{WC}(s) = s^2 + 2\xi_{CL}^{WC}\omega_{CL}^{WC} s + \left(\omega_{CL}^{WC}\right)^2 \tag{53}$$

with:

$$\begin{aligned} \omega_{CL}^{WC} &= \sqrt{-\omega_{PV\min} R_{I\min} K_I} = \sqrt{C_I^{-1} K_I} \\ \xi_{CL}^{WC} &= \frac{\omega_{PV\min}\left(1 - R_{I\min} K_P\right)}{2\sqrt{-\omega_{PV\min} R_{I\min} K_I}} = \frac{C_I^{-1}\left(K_P - I_{SC} V_{\min}^{-1}\right)}{2\sqrt{C_I^{-1} K_I}}. \end{aligned} \tag{54}$$

On the other hand, according to Equation (24):

$$\omega_{PV\max} = \left(C_I R_S\right)^{-1} = \left(C_I R_{PV\min}\right)^{-1} \tag{55}$$

and the corresponding "best case" plant is given by:

$$H_{IV}^{BC}(s) = \frac{R_{PV\min}}{\omega_{PV\max}^{-1} s + 1}. \tag{56}$$

Hence, under control law given by Equation (50), the following closed-loop tracking response is expected:

$$T_I^{CL}(s) = \frac{\omega_{PV\max} R_{PV\min}\left(K_P s + K_I\right)}{s^2 + \omega_{PV\max}\left(1 + R_{PV\min} K_P\right) s + \omega_{PV\max} R_{PV\min} K_I}. \tag{57}$$

The denominator of Equation (57) may be rewritten as:

$$\Delta_{CL}^{BC}(s) = s^2 + 2\xi_{CL}^{BC}\omega_{CL}^{BC} s + \left(\omega_{CL}^{BC}\right)^2 \tag{58}$$

with:

$$\begin{aligned} \omega_{CL}^{BC} &= \sqrt{\omega_{PV\max} R_{PV\min} K_I} = \sqrt{C_I^{-1} K_I} \\ \xi_{CL}^{BC} &= \frac{\omega_{PV\max}\left(1 + R_{PV\min} K_P\right)}{2\sqrt{\omega_{PV\max} R_{PV\min} K_I}} = \frac{C_I^{-1}\left(K_P + R_S^{-1}\right)}{2\sqrt{C_I^{-1} K_I}}. \end{aligned} \tag{59}$$

Comparison of Equations (54) and (59) reveals that while the natural frequency remains unchanged, damping is expected to increase when moving from the "worst case" (close to short-circuit conditions) to the best case (open circuit conditions), resembling the performance of SA-interfacing current-controlled

boost converter reported in [10], where no open-loop instability occurs. Consequently, under the proposed control buck power stage is expected to perform similarly to SA-interfacing boost power stage.

5. Demonstration

A PSIM software-based simulation study is performed next to verify the revealed findings. Experimental case study and implementation issues are reported separately in [32]. Consider a BP-Solar MSX-60 solar array with Standard Test Conditions (STC) data summarized in Table 1 and corresponding I-V and P-V curves shown in Figure 18, interfaced by two identical current-mode-controlled buck converters with $C_I = C_O = 470$ μF and $L = 10$ μH. The converters are feeding two 3-Cell Li-Ion batteries (terminal voltage may vary between 9 and 12.6 V) with 150 mΩ internal resistance. Initial terminal voltages of the batteries are set to 9 and 12 V, respectively, to indicate different initial state of charge. Simulation circuit diagram is shown in Figure 19.

Table 1. BP-Solar MSX-60 solar array standard test conditions (STC) performance.

Parameter	Value
Open circuit voltage	21.1 V
Short circuit current	3.8 A
Maximum power voltage	17.1 V
Maximum power current	3.5 A
Rated power	60 W
Power temperature coefficient	−0.5%/°C
Voltage temperature coefficient	−80 mV/°C
Current temperature coefficient	0.065%/°C

In order to demonstrate two static-instability issues, related to non-MPP operation (addressed in Section 2), inductor current reference was set such that total charging power of both batteries was ~39 W. According to the characteristic curves of SA under study, two possible operating points exist: (10.3 V, 3.8 A) on the left of MPP and (19.7 V, 2 A) on the right of MPP, as shown in Figure 18. In order to demonstrate the instability of the operating point residing on the left of MPP, voltage open-loop simulations were carried out for four different initial values of SA terminal voltages: 9.5 V (slightly lower than 10.3 V), 11 V (slightly higher than 10.3 V), 19 V (slightly lower than 19.7 V) and 20.5 V (slightly higher than 19.7 V). Time-domain curves of SA voltages, currents and power for all the four initial conditions are shown in Figure 20. Apparently, in all the four cases the system settles at the operating point residing on the right of MPP, indicating its static stability.

In order to demonstrate operating point loss, the system was first brought to the stable operating point determined above and then irradiation level was reduced in a step-like manner from 1000 W m^{-2} to 500 W m^{-2} at $t = 3$ ms. The results are shown in Figure 21. Apparently, the SA is incapable of generating 39 W at half-STC irradiation. Consequently, its output voltage collapses and operation point is lost.

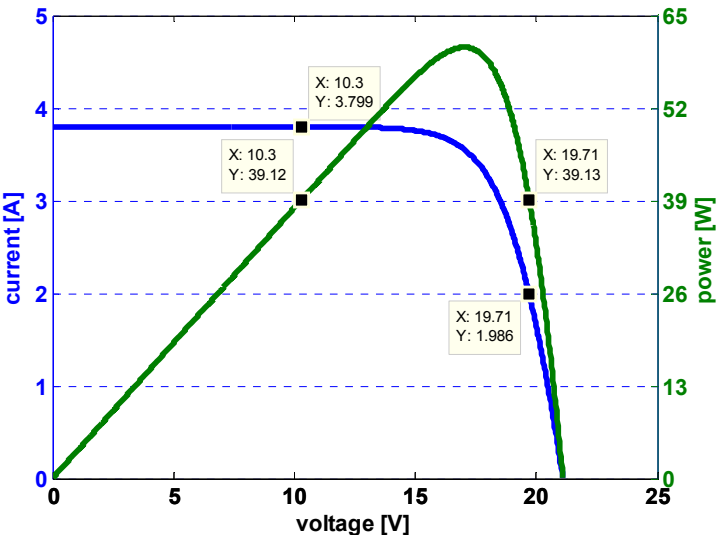

Figure 18. I-V and P-V standard test conditions (STC) curves of BP-Solar MSX-60 solar array.

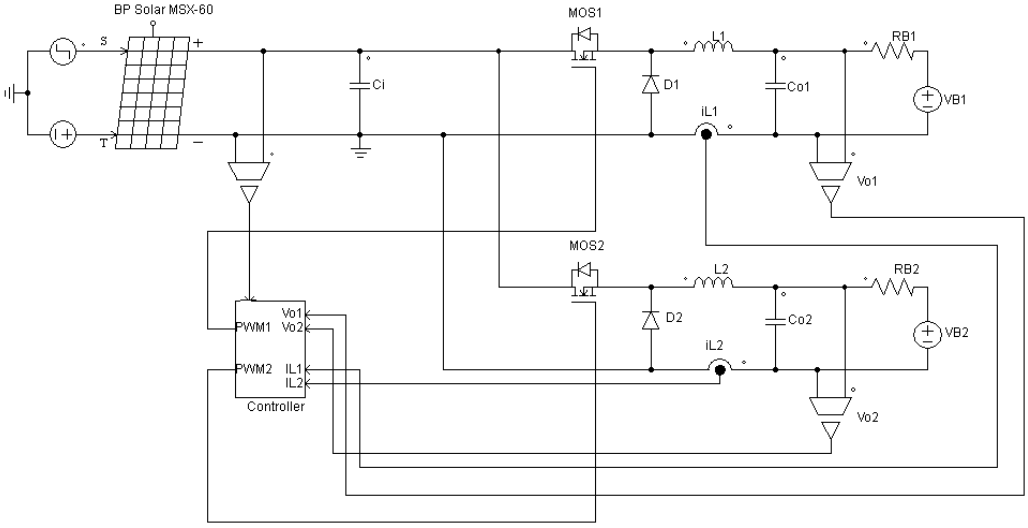

Figure 19. PSIM software simulation circuit diagram.

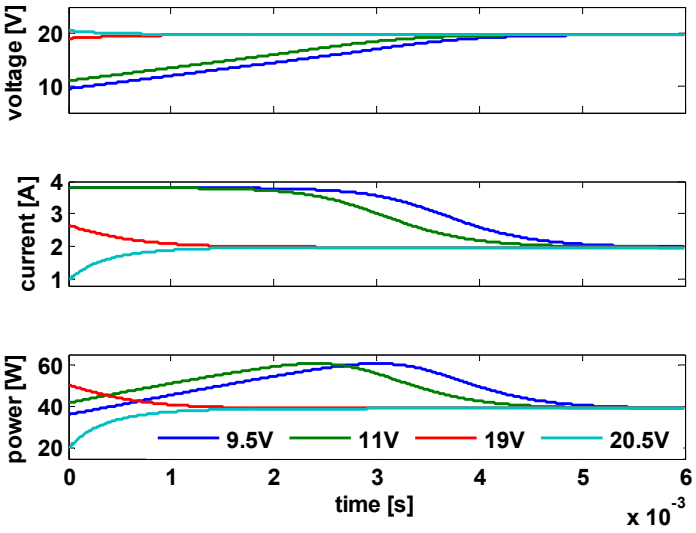

Figure 20. Voltage open-loop system behavior for different initial values of SA terminal voltage.

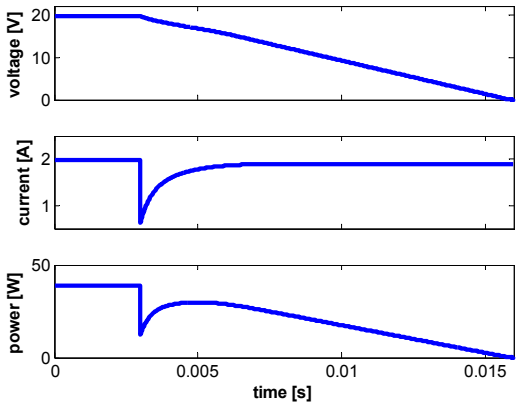

Figure 21. Operation point loss as a result of abrupt irradiation decrease.

Taking into account battery terminal voltage range, in order to ensure correct operation of buck topology minimum SA voltage is set to 14 V. Consequently, SA voltage may vary from 14 to 21.1V and the duty cycle of each converter resides in $0.43 < D < 0.9$ region. According to Equations (21), (24) and Equation (49), the worst case plant is given by:

$$H_{IV}^{WC}(s) = \frac{\frac{14}{3.8}}{1 - 470 \cdot 10^{-6} \frac{14}{3.8} s} = \frac{3.68}{1 - 1.73 \cdot 10^{-3} s} = \frac{3.68}{1 - \frac{s}{577.5}}, \tag{60}$$

i.e., the worst case unstable pole resides at 577.5 rad/s. Selecting a PI controller Equation (50) for loop compensation results in the following closed loop transfer function:

$$T_I^{CL}(s) \overset{\Delta}{=} \frac{\tilde{v}_I}{\tilde{v}_I^*}(s)\bigg|_{\tilde{f}(s)=0} = \frac{577.5 \cdot 3.8 \cdot \left(K_P s + K_I\right)}{s^2 - 577.5\left(1 - 3.8K_P\right)s + 577.5 \cdot 3.8 \cdot K_I}. \tag{61}$$

Selecting $K_I = 1822$ and $K_P = 1.17$ leads to a stable closed loop transfer function with:

$$\omega_{CL}^{WC} = 2000\text{rad/s} \quad \xi_{CL}^{WC} = 0.5 \tag{62}$$

In order to validate the revealed findings, closed-loop system simulation was carried out as follows: reference input voltage signal v_I^* was reduced by steps of 1 from 21 V (nearly open-circuit conditions) down to 14 V (minimum allowed SA voltage) and dynamic SA terminal voltage response was recorded. The simulation was run twice: first with the above derived PI controller coefficients (ensuring stability) and second with the same K_I yet 10 times smaller K_P of 0.117, yielding instability on the left of MPP. The results are given in Figure 22. As expected, while the response using $K_P = 1.17$ is stable at all operating points, differing by damping only, system behavior for $K_P = 0.117$ becomes unstable for input voltages below 17.1 V (MPP).

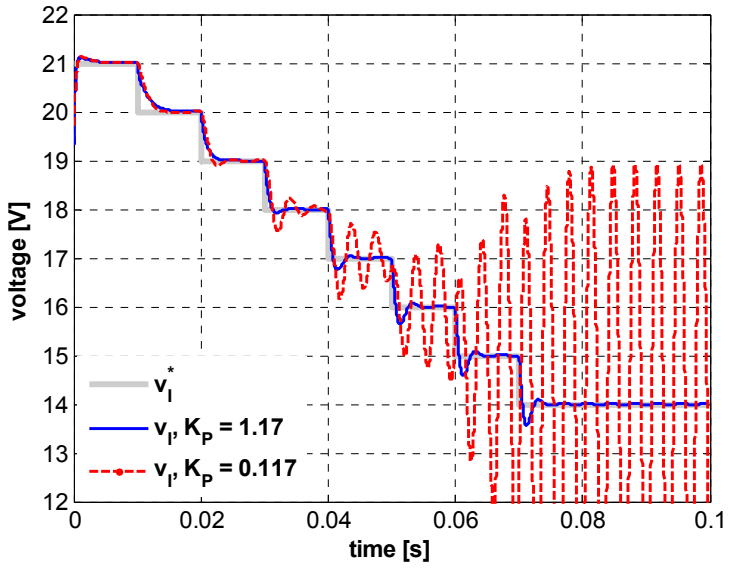

Figure 22. Closed-loop input voltage responses for different K_P.

6. Conclusions

In this paper, dynamic analysis of a multi-battery charger suitable for lead-acid and lithium-ion cell-based batteries and connected to a single solar array was carried out, revealing several stability-related issues. Current-controlled buck power stages were assumed as power-processing interfaces, powering batteries operating either in constant power or constant voltage mode, implying input or output voltage converter regulation, respectively. While output-voltage control loops analysis was shown to be trivial in case suitable static operating point exists, input-voltage control dynamics turned out to be problematic. It was revealed that constant power charging mode may lead to open-loop instability whenever solar array voltage is lower than its maximum power point voltage. Therefore, the design of input voltage regulating controller must be carried out to stabilize the closed-loop dynamics for the worst case of instability, which is also quantified in the paper. Moreover, it was shown that the output voltage control dynamics are "seen" as disturbances by input voltage control loop; thus input voltage controller must be capable of rejecting these. Simple PI structure-based stabilizing controller design was proposed, allowing both attaining stable closed-loop system in case of worst case instability and attenuating output voltage control induced disturbances. The main drawback of the proposed control method is operating-point dependent closed-loop damping, leading to non-constant closed loop transient behavior. Revealed findings were validated through extended detailed simulations.

Author Contributions

M.A. conceived and designed the simulations; M.S. and S.G. analyzed the data; T.S. and A.K. contributed analysis tools; A.K. wrote the paper.

Conflicts of Interest

The authors declare no conflict of interest.

Abbreviations

SA—Solar array
PWM—Pulse Width Modulation
IC—Integrated Circuit
MPP—Maximum Power Point
MPPT—Maximum Power Point Tracking
LPP—Limited Power Point
CP—Constant Power
CV—Constant Voltage
CMC—Current Mode Control
PI—Proportional Integrative

Nomenclature

P_B —battery power
P_{PV} —solar array power
P_I —converter input power
R_{BAT} —battery equivalent series resistance
V_{BAT} —battery electro-motive force
I_{PH} —solar array photocurrent
I_O —solar array reverse saturation current
V_T —solar array thermal voltage
a —solar array ideality factor
R_S —solar array series resistance
R_P —solar array shunt resistance
v_O —converter output voltage
i_O —converter output current
v_I —converter input voltage
i_I —converter input current
i_L —converter inductor current
C_I —converter input capacitance
C_O —converter output capacitance
D —converter duty cycle
η —converter efficiency
x^* —reference value of variable x
$\tilde{x}$ —small-signal value of variable x
X —steady-state value of variable x

References

1. Bragard, M.; Soltau, N.; Thomas, S.; De Doncker, R.W. The balance of renewable sources and user demands in grids: Power electronics for modular battery energy storage systems. *IEEE Trans. Power Electron.* **2010**, *25*, 3049–3056.
2. Zhou, H.; Bhattacharya, T.; Tran, D.; Siew, T.S.T.; Khambadkone, A.M. Composite energy storage system involving battery and ultracapacitor with dynamic energy management in microgrid applications. *IEEE Trans. Power Electron.***2011**, *26*, 923–930.
3. Sun, K.; Zhang, L.; Xing, Y.; Guerrero, J. A distributed control strategy based on DC bus signaling for modular photovoltaic generation systems with battery energy storage. *IEEE Trans. Power Electron.* **2011**, *26*, 3032–3045.
4. Locment, F.; Sechilariu, M.; Houssamo, I. DC load and battery control limitations for photovoltaic systems. Experimental validation. *IEEE Trans. Power Electron.* **2012**, *27*, 4030–4038.
5. Dragicevic, T.; Guerrero, J.; Vasquez, J.; Skrlec, D. Supervisory control of an adaptive-droop regulated DC microgrid with battery management capability. *IEEE Trans. Power Electron.* **2013**, *29*, 695–706.
6. Fakham, H.; Lu, D.; Francois, B. Power control design of a battery charger in a hybrid active PV generator for load-following applications. *IEEE Trans. Ind. Electron*. **2011**, *58*, 85–94.
7. Indu Rani, B.; Sravana Ilango, G.; Nagami, C. Control strategy for power flow management in a PV system supplying DC loads. *IEEE Trans. Ind. Electron*. **2013**, *60*, 3185–3194.
8. Aharon, I.; Kuperman, A. Topological overview of battery powered vehicles with range extenders. *IEEE Trans. Power Electron.* **2011**, *26*, 868–876.
9. Gadelovits, S.; Kuperman, A.; Sitbon, M.; Aharon, I.; Singer, S. Interfacing renewable energy sources for maximum power transfer—Part I: Statics. *Renew. Sustain. Energy Rev*. **2014**, *31*, 501–508.
10. Urtasun, A.; Sanchis, P.; Marroyo, L. Adaptive voltage control of the DC/DC boost stage in PV converters with small input capacitor. *IEEE Trans. Power Electron*. **2013**, *28*, 5038–5048.
11. Lu, D.; Agelidis, V. Photovoltaic-battery-powered DC bus system for common portable electronic devices. *IEEE Trans. Power Electron.* **2009**, *24*, 849–855.
12. Ongaro, F.; Saggini, S.; Mattavelli, P. Li-Ion battery-supercapacitor hybrid storage system for a long lifetime, photovoltaic-based wireless sensor network. *IEEE Trans. Power Electron.* **2012**, *27*, 3944–3952.
13. Kim, H.; Parkhideh, B.; Bongers, T.; Gao, H. Reconfigurable solar converter: A single-stage power conversion PV-battery system. *IEEE Trans. Power Electron.* **2013**, *28*, 3788–3797.
14. Barreto, L.; Praca, P.; Oliveira, D.; Silva, R. High-voltage gain boost converter based on three-state commutation cell for battery charging using PV panels in a single conversion stage. *IEEE Trans. Power Electron.* **2014**, *29*, 150–158.
15. Harrington, S.; Dunlop, J. Battery charge controller characteristics in photovoltaic systems. *IEEE Aerosp. Electron. Syst. Mag.* **1992**, *7*, 15–21.
16. Boico, F.; Lehman, B.; Shujaee, K. Solar battery charger for NiMH batteries. *IEEE Trans. Power Electron*. **2007**, *22*, 1600–1609.

17. Carli, G.; Williamson, S. Technical considerations on power conversion for electric and plug-in hybrid electric vehicle battery charging in photovoltaic installations. *IEEE Trans. Power Electron.* **2013**, *28*, 5784–5792.
18. Siri, K. Study of system instability in solar-array-based power systems. *IEEE Trans. Aerosp. Electron. Syst*. **2000**, *36*, 957–964.
19. Leppaaho, J.; Suntio, T. Characterizing the dynamics of the peak-current-mode-controlled buck power stage converter in photovoltaic applications. *IEEE Trans. Power Electron.* **2014**, *29*, 3840–3847.
20. Vesti, S.; Suntio, T.; Oliver, J.; Prieto, R.; Cobos, J. Effect of control method on impedance-based interactions in a buck converter. *IEEE Trans. Power Electron.* **2013**, *28*, 5311–5322.
21. Anand, S.; Fernandes, B.; Guerrero, M. Distributed control to ensure proportional load-sharing and improve voltage regulation in low-voltage DC microgrids. *IEEE Trans. Power Electron*. **2013**, *28*, 1900–1913.
22. He, J.; Li, Y.-W. An enhanced microgrid load demand sharing strategy. *IEEE Trans. Power Electron*. **2012**, *27*, 3984–3995.
23. Urayai, C.; Amaratunga, G.A.J. Single-sensor maximum power point tracking algorithms. *IET Renew. Power Gener*. **2013**, *7*, 82–88.
24. Shmilovitz, D. On the control of photovoltaic maximum power point tracker via output parameters. *IEE Proc. Electr. Power Appl*. **2005**, *152*, 239–248.
25. Kuperman, A.; Levy, U.; Goren, J.; Zafransky, A.; Savernin, A. Battery charger for electric vehicle traction battery switch station. *IEEE Trans. Ind. Electron*. **2013**, *12*, 5391–5399.
26. Lineykin, S.; Averbukh, M.; Kuperman, A. An improved approach to extracting the single-diode equivalent circuit parameters of a photovoltaic cell/panel. *Renew. Sustain. Energy Rev.* **2014**, *30*, 282–289.
27. Lineykin, S.; Averbukh, M.; Kuperman, A. Issues in modeling amorphous silicon photovoltaic modules by single-diode equivalent circuit. *IEEE Trans. Ind. Electron.* **2014**, *61*, 6785–6793.
28. Nousiainen, L.; Puukko, J.; Maki, A.; Messo, T.; Huusari, J.; Jokipii, J.; Viinamaki, J.; Lobera, D.T.; Valkealahti, S.; Suntio, T. Photovoltaic generator as an input source for power electronic converters. *IEEE Trans. Power Electron*. **2013**, *28*, 3028–3038.
29. Pavlovic, T.; Bjazic, T.; Ban, Z. Simplified averaged models of DC-DC power converters suitable for controller design and microgrid simulation. *IEEE Trans. Power Electron.* **2013**, *28*, 3266–3275.
30. Kuperman, A. Comments on "An analytical solution for tracking photovoltaic module MPP". *IEEE J. Photovolt.* **2014**, *4*, 734–735.
31. Messo, T.; Jokipii, J.; Puukko, J.; Suntio, T. Determining the value of DC-link capacitance to ensure stable operation of a three-phase photovoltaic inverter. *IEEE Trans. Power Electron.* **2014**, *29*, 665–673.
32. Gadelovits, S.; Sitbon, M.; Suntio, T.; Kuperman, A. Single-source multi-battery solar charger: Case study and implementation issues. *Prog. Photovolt. Res. Appl*. **2015**, doi:10.1002/pip.2591.

© 2015 by the authors; licensee MDPI, Basel, Switzerland. This article is an open access article distributed under the terms and conditions of the Creative Commons Attribution license (http://creativecommons.org/licenses/by/4.0/).